EFFECTS OF ENVIRONMENTAL SHEAR AND BUOYANCY ON SIMULATED SUPERCELL INTERACTIONS

BY

NATHAN ALLEN WENDT

THESIS

Submitted in partial fulfillment of the requirements
for the degree of Master of Science in Atmospheric Sciences
in the Graduate College of the
University of Illinois at Urbana-Champaign, 2015

Urbana, Illinois

Master's Committee:

Professor Robert M. Rauber
Research Scientist Brian F. Jewett

Abstract

This study examines the role that buoyancy and vertical wind shear play in modulating the relationship between storm interactions and storm severity. Using an idealized numerical model, 240 supercell interactions are simulated under systematically varied amounts of buoyancy and vertical wind shear. Small changes in buoyancy or vertical wind shear have significant impacts on post-interaction storm morphology. A wide amount of variation in low-level rotation is seen across the simulation suite. Two-cell storm simulations are not always stronger than one-cell control simulations. Migration of low-level vertical vorticity centers is ubiquitous through all runs, but orientation of and interaction between two storms' gust fronts modulates where the vorticity center will end up. Gust fronts in better alignment have more vorticity centers reach an updraft where they are stretched and intensified. With respect to storm mode, higher buoyancy produced less classic supercells while higher shear produced more classic supercells. High precipitation supercells were favored with two-cell simulations where the second cell was directly to the southwest of the control cell. Secondary cells that were close to the control merged quickly and were often stronger than simulations with large cell separation distance. Further questions remain with trajectories and machine learning algorithms are tthe next steps for a more detailed analysis of this large data set.

To my wife and children

Acknowledgments

First, many thanks are due to my wife, children, and other family members. Their support during this period of my career was very important to my success. They worked at least as hard as I did to make this happen.

A special thanks also is due to my advisor, Brian Jewett. The beast that is numerical modeling of convective weather is hard to tame. I appreciate his advice that has helped take my big ideas and turn them into tractable problems to try and solve. I look forward to future collaboration with him on some of the exciting questions that still remain unanswered in the science of atmospheric convection.

I would also like to acknowledge the staff at the Texas Advance Computing Center. The use of their Stampede supercomputer (under XSEDE award TG-ATM050014N) was an integral part of this project. I appreciate their help making things run smoothly.

The faculty and staff at the UIUC Department of Atmospheric Sciences deserves recognition. Th financial support provided by the Department made my time at UIUC possible. I thank them all for thet opportunity to pursue a graduate degree within the Department and for the knowledge that they have shared over the course of my studies. I have gained a great deal of useful skills through their instruction and am confident in being able to contribute to the Atmospheric Sciences field throughout my career.

Lastly, I would like to thank the many students that I interacted with on a regular basis during my time at UIUC. Some of you I shared an office with, others not, but you know who you are. Being able to bounce ideas off of one another or simply just relax and have some fun made the graduate school experience a great deal more pleasant.

Table of Contents

List of Abbreviations

AGL	Above ground level
CAPE	Convective available potential energy
CIN	Convective inhibition
CL	Classic supercell
FFGF	Forward flank gust front
HP	High-precipitation supercell
LCL	Lifted condensation layer
LN	Linear storm mode
ML	Mixed layer
PBL	Planetary boundary layer
QSC	Quarter semicircle
SRH	Storm-relative helicity

List of Symbols

a	Radian measure of hodograph curvature
c_p	Specific heat at constant pressure
d_c	Depth of hodograph curvature
g	Gravitational constant
S_u	Shape parameter of the u wind component
S_v	Shape parameter of the v wind component
T_{tr}	Temperature at the tropopause
$\bar{\theta}$	Mean potential temperature
θ_0	Surface potential temperature
θ_{ml}	Potential temperature at the height of the mixed layer
θ_{tr}	Potential temperature at the tropopause
$\frac{\partial\theta}{\partial z}$	Potential temperature lapse rate
u	Zonal wind speed
u_{sfc}	Zonal surface wind speed.
U_s	Zonal vertical wind shear magnitude
v	Meridional wind speed
v_{sfc}	Meridional surface wind speed
V_s	Meridional vertical wind shear magnitude
z	AGL height
z_{ml}	Height of the mixed layer
z_{tr}	Height of the tropopause

1 Introduction

The interactions between two or more convective cells can be broadly classified into two groups: interactions between storms' outflows and merging of storms' reflectivity cores. Of course, there can be overlap between these two groups as well. These interactions have important consequences for storm morphology and severity (e.g., Goodman and Knupp, 1993; Lee et al., 2006; Wurman et al., 2007; French and Parker, 2012; Van Leer, 2012). Changes in a storm's morphology or severity are of particular importance to operational meteorologists—particularly when these changes occur on small time scales.

Both observational and numerical modeling studies have been previously carried out to investigate storm interactions. Observational data on storm interactions most often comes from radars and surface stations used during field campaigns or operationally. From these studies, we see that there is often a correlation between cell interactions or mergers and tornadogenesis (Lee et al., 2006; Wurman et al., 2007) or mesocyclone intensification (Hastings et al., 2010). Another common finding is that outflow boundaries from one storm interact with outflow boundaries of another storm leading to locally enhanced convergence (Goodman and Knupp, 1993; Wolf and Szoke, 1996; Gilmore and Fox, 2005; Wurman et al., 2007; Rogers and Weiss, 2008; French and Parker, 2012). There is also some indication that the location of one storm relative to another impacts the outcome of any interaction or merger (Rogers and Weiss, 2008; Rogers, 2012). Specifically, mergers and interactions along the flanking line tended to show increases in storm inten-

sity, whereas storms that interacted or merged with another storms inflow region showed decreases in intensity (Lindsey and Bunkers, 2004; Gilmore and Fox, 2005). What these observational studies are often lacking is concrete evidence of the physical link between the interacting or merging cells. These limitations are, in part, due to the inability of most of these observation platforms to gather data at the requisite spatial (horizontal and vertical) and temporal resolutions.

Numerical studies have been the primary tool of researchers to get an improved picture of the process of convective cell interactions. Models give one the ability to output nearly any variable at high spatial and temporal resolutions. These studies have done a great deal in terms of advancing the science of storm interactions and mergers. Bluestein and Weisman (2000) showed how varying the shear vector with respect to an initiating boundary changed the potential for storm mergers and overall evolution of the system. Other studies have noted that the relative location of one storm to another, the timing of the interaction, and the intensity of the interacting storms play a role in modulating the outcome of the interaction (Jewett et al., 2002, 2006; Hastings and Richardson, 2010; Syrowski et al., 2012). In particular, these studies have indicated that, under westerly shear, the interactions most likely to result in intensification occur when one cell is southwest of the other cell. In these cases, the secondary cell to southwest sheds its left-mover into the cold pool of the primary cell, not allowing it to destructively interfere with the primary cell (Rotunno et al., 1988). Of the studies that have investigated the dominant physical processes at work in mergers, it has been generally shown that tilting of horizontal vorticity by downdrafts in rear- and forward-flanks of a storm undergo some amount of stretching and intensification either by convergence along a surface boundary, being ingested into the parent updraft,

or both (Syrowski et al., 2012; Hastings et al., 2012, 2014).

Tanamachi et al. (2015) also showed that vertical vorticity can increase in the midlevels during interactions as well. By assimilating data from a phased array radar into a numerical model, Tanamachi et al. showed how a less mature storm merged with a mature supercell and caused new updraft to form between the two storms (called bridging updrafts, see Tao and Simpson 1989; Wurman et al. 2007). These new updrafts tilted ambient horizontal vorticity into the vertical and this new area of midlevel, cyclonic rotation merged with and helped strengthen the midlevel, cyclonic rotation of the mature supercell.

One limitation of the extant numerical studies on storm interactions is that they typically only use one or two vertical wind profiles and only one vertical buoyancy profile. These vertical profiles are either taken from operational forecast models (from an nearby location representative of a storm's inflow) prior to a real event or from other idealized storm studies, most often Weisman and Klemp (1982) and Weisman and Klemp (1984).

Supercells exist within environments that tend to have particular properties. Several studies (e.g., Doswell et al., 1993; Rasmussen and Blanchard, 1998; Rasmussen, 2003; Thompson et al., 2003; Grams et al., 2011) have detailed the environmental characteristics that are associated with supercells. Note that, for this work, the typical values of any parameter are taken to be representative of the Great Plains region during Spring. Of all the parameters, convective available potential energy (CAPE) and 0–6 km bulk shear are the most commonly referenced. CAPE is simply the amount of positive buoyancy available to the rising parcel of air. The warmer the parcel of air as it rises relative to the ambient environment, the more CAPE exists in that environment for that parcel. Adequate CAPE ($\geq$ 1500 Jkg^{-1}) is necessary

for strong enough updrafts in supercells. The 0–6 km (or deep-layer) bulk shear is a measure that is often used to predict what the dominant storm type in an environment will be and is essentially the vector wind difference between the surface and 6 km aloft. Higher magnitudes of 0–6 km bulk shear ($\geq$ 20 ms^{-1}) are associated with supercells. Lastly, storm-relative helicity (SRH; Davies-Jones, 1984) is also used when characterizing supercell environments. SRH refers to the amount of streamwise vorticity—the component of vorticity parallel to the storm's inflow—available to be ingested by the storm. This quantity is related to the amount of directional turning (in this case clockwise) with height of the environmental shear vector. Values of SRH in the 0–3 km layer that exceed 100 m^{2}s^{-2} are indicative of potential for supercells. SRH is also used a predictor for tornado potential as well.

The objective of the current study is to expand on previous work, outlined above, by varying both the vertical wind profile and the vertical buoyancy profile. What remains unknown are how changes in environmental buoyancy and shear might change the relationships between storm interaction, morphology, and intensity. By adding these variations, we hope to answer questions about how instability and vertical shear modulate the relationship between thunderstorm interaction and storm structure and evolution. Chapter 2 describes the methods used to answer the research questions. Chapter 3 details the results of numerical simulations. Finally, chapter 4 will discuss and offer conclusions based on the findings.

2 Methodology

2.1 Idealized simulations

In the real atmosphere, there are several environmental properties associated with severe thunderstorms, such as buoyancy and shear, that can be summarized using certain metrics. Such metrics include CAPE, 0–6 km bulk shear, and SRH. In order to study the effects of changes in these metrics, idealized models can be employed. As part of idealized simulations, these metrics can be systematically altered and inserted into the simulated atmosphere through, in the case of these metrics, an input sounding. That is to say, the input sounding is modified by the user and used by the model as an initial condition for the simulated atmosphere. When several of these metrics are modified over the course of many idealized simulations, it is often referred to as a parameter study. The data produced by these parameter studies are investigated to understand how and why small changes in a given metric has a particular effect on the evolution of the modeled storm or storms. In the past, parameter studies involving supercells have been done using idealized models (McCaul and Weisman, 2001; Syrowski et al., 2012). This study also makes use of the parameter study framework to understand the changes in storm severity and morphology induced by changing metrics within the simulated environment of interacting supercells. Here our parameter space, all the possible simulated environments applied in the model, will be defined by varying combinations of CAPE, low-level hodograph curvature (i.e., changes

in SRH), and secondary storm location.

2.1.1 Model configuration

The idealized simulations of storm interactions in this study used version 3.5.1 of the Weather Research & Forecasting model (WRF; Skamarock et al., 2008) with the Advanced Research dynamical core. All simulations were carried out on a 256×280×120 Arakawa C-grid (Arakawa and Lamb, 1977) with a 3 s time step, 540 m horizontal grid spacing, and a stretched vertical grid up to 20 km. An outer grid was placed outside the main domain to help eliminate waves along the 540 m main grid boundaries. While this is a nested-grid simulation, only the innermost grid will be used for analysis. An overview of the physics and dynamics options used for these idealized runs can be found in Table 2.1.

The choice of the Morrison, two-moment microphysics scheme was due to the fact that simulated supercell presentation was more realistic than with other tested microphysics schemes. This study has changed the dominant ice category in the Morrison microphysics scheme to hail—the default being graupel. It is a recommended change for continental, deep convection and certainly characteristic of supercell thunderstorms. Other studies have made changes to the Morrison scheme. For example, Hastings (2013) found that nearly all interactions behaved similarly when the cutoff diameter (having to do with collision-collection efficiency; see Morrison et al. (2005)) was changed from the default 0.3 mm to 0.6 mm. However, a small subset of interactions did evolve differently and showed differences in low-level vorticity fields. All of these things considered, it appears justifiable to limit this study to the default Morrison formulation (along with the hail change noted above).

Through experimentation, it was found that many of the simulations de-

veloped noisy looking reflectivity fields; in particular, this occurred along the inflow boundary. Several strategies were employed to reduce this numerical noise within the model. One of them, mentioned above, was to use a nested simulation. Since the waves developed along the edge of inflow boundaries, pushing that inflow boundary away from the nest effectively removed the influence of the waves on the simulated storms in the nest. A w-Rayleigh damping scheme was also used to eliminate waves being generated at the domain top by strong convective updrafts. Within the model, the tropopause is specified to be 12 km. With that in mind, the w-damping depth was set to 5 km from the model top of 20 km. This will still allow for the overshooting tops of severe convection as observations have shown that these overshooting tops are typically only a few kilometers above the cloud top (Heymsfield et al., 1991). Lastly, a 6th order diffusion scheme was also employed to help curtail spurious waves. It is known that small perturbations can grow larger in nearly-neutral or unstable boundary layers (Knievel et al., 2007). The input soundings for these simuations contain boundary layers that are nearly neutral; as such, it makes sense to utilize the model's 6th order diffusion scheme.

2.1.2 Vertical wind profiles

As was mentioned, supercells exist within environments that have a specific vertical wind profile. A typical supercellular environment has a hodograph much like the one in Figure 2.1. The notable features of this hodograph are the long length and the clockwise curvature below 2 km AGL. The long nature of the hodograph implies larger deep-layer shear values. The 0–6 km bulk shear in this case is greater than 30 ms^{-1}. The low-level curvature implies a larger SRH value, particularly since the storm motion is well off of

the hodograph[1].

The matrix of simulations that were done in this study were initialized with one of five different hodographs (Figure 2.2). The hodographs were created using a modified version of the hodographs used in Weisman and Klemp (1984). Care was also taken to match 0–6 km bulk shear, 0–3 km storm-relative helicity (SRH), 0–1 km SRH, surface winds, and overall shape as close as possible to climatological values for supercell environments (see Thompson et al., 2003; Grams et al., 2011; Parker, 2014). Ultimately, the goal is to simulate supercellular thunderstorms. To do this, 0–6 km bulk shear must be high enough to produce supercells. Given that, the 0–6 km bulk shear is kept nearly constant so that incremental changes in the low-level hodograph curvature can be used to explain variation in storm intensity and morphology. The decision to only modify the low-level ($z \leq 1.5$ km) hodograph curvature is based on prior research showing the important of this shear depth in low-level rotation (Thompson et al., 2003).

Figure 2.1 gives a hodograph containing several nice features that can be generalized and controlled using an analytic equation. Through the analytic equation, the properties of the hodograph (e.g., SRH) can be incrementally changed such that changes in simulation behavior can be tied to those changes. Furthermore, the analytic expression used for the hodograph can be built in such a way that other properties are conserved or nearly conserved (e.g., 0–6 km bulk shear). What follows is a description of the analytic expressions used to create input hodographs for the idealized simulations.

Equations 2.1 and 2.2 are the zonal and meridional equations for the

[1]SRH is proportional to the area swept out by tracing a line from the storm motion to the surface and to a given depth (usually 3 km). The farther the storm motion is "off of the hodograph", the more area will be swept out. Thus, a higher SRH value will be observed.

vertical wind profile, respectively.

$$u(z) = u_{sfc} + S_u U_s - S_u U_s cos\left(\frac{az\pi}{d_c}\right) \tag{2.1}$$

$$v(z) = v_{sfc} + S_v V_s sin\left(\frac{az\pi}{d_c}\right) \tag{2.2}$$

Here u is the zonal wind speed, v is the meridional wind speed, u_{sfc} is the zonal surface wind speed, v_{sfc} is the meridional wind speed, U_s is the zonal vertical wind shear magnitude, V_s is the meridional vertical wind shear magnitude, and z is the AGL height. The parameters S_u and S_v are the zonal and meridional shape factors of the hodograph, respectively. They control the overall curvature. For reference, $S_u = S_v$ would produce a fully circular hodograph through a given depth. The other important parameters are a, the radian measure of hodograph curvature, and d_c, the depth of hodograph curvature. These parameters control the angle and depth through which the hodograph curves, respectively. Equations 2.1 and 2.2 are used to construct the hodograph up to the curvature depth, d_c. For this study, $d_c = 1.5$ km for all idealized simulations. Beyond 1.5 km, the u-component of the wind increases linearly up to 6 km where the full velocity is then held constant thereafter, similar to Weisman and Rotunno (2000). Table 2.2 shows the parameters used in this study.

The five hodographs in Figure 2.2 range from a straight line to a quarter-semicircle (QSC). Bulk shear in the 0–6 km layer ranged from 25 m s^{-1} in the straight hodograph case to 26.9 m s^{-1} in the QSC case. This negligible difference should not impact interpretation of results and these values are within the typical range for southern plains supercells in the spring season (Thompson et al., 2003; Grams et al., 2011). Surface winds are southeasterly at 6.4 m s^{-1}, comparable to observations (Parker, 2014). SRH for these

hodographs for 0–3 km (0–1 km) are found in Table 2.2. Most of these SRH values fall within the range of tornadic storms on the plains (Thompson et al., 2003). The cases of 0 and 0.125 shape factors can be considered edge cases in that, particularly the 0–1 km depth, their SRH values are somewhat low. However, these edge cases with borderline SRH parameters offer the chance to see if storm interactions play a role in amplifying storm intensity beyond what parameters would indicate possible. Hence, they still offer value. The storm motions used in the SRH calculations were taken to be the mean storm motion between $t = 2$ hours and $t = 3$ hours in test simulations for each vertical wind profile.

2.1.3 Vertical thermodynamic profiles

Perhaps the most referenced thermodynamic profiles in the numerically simulated storm literature is found in Weisman and Klemp (1982). The thermodynamic profile they used was made using an analytic expressions that gave smooth temperature and moisture profiles as well as having a nearly well-mixed PBL, small CIN, and relatively low LCLs. The vertical thermodynamic profiles used in this study were created using the same analytic expressions for temperature and relative humidity as Weisman and Klemp with a few modifications. The temperature profile in these simulations is defined by

$$\bar{\theta}(z) = \begin{cases} \theta_0 + z\frac{\partial\theta}{\partial z}, & z \leq z_{ml} \\ \theta_{ml} + (\theta_{tr} - \theta_{ml})\left(\frac{z - z_{ml}}{z_{tr} - z_{ml}}\right)^{5/4}, & z_{ml} < z \leq z_{tr} \\ \theta_{tr}\, exp\left[\frac{g}{c_p T_{tr}}(z - z_{tr})\right], & z > z_{tr} \end{cases} \tag{2.3}$$

where $\bar{\theta}$ is the mean potential temperature, θ_0 is the surface potential temperature, z is the AGL height, $\frac{\partial\theta}{\partial z}$ is the potential temperature lapse rate, z_{ml} is the height of mixed layer, θ_{ml} is the potential temperature at the mixed layer height, θ_{tr} is the potential temperature at the tropopause, z_{tr} is the height of the tropopause, g is the gravitational constant, c_p is the specific heat at constant pressure, and T_{tr} is the temperature at the tropopause. Values of θ_0, θ_{tr}, z_{tr}, and T_{tr} are taken from Weisman and Klemp (1982).

In equation 2.3, the main departure from Weisman and Klemp (1982) and Weisman and Klemp (1984) is that the lapse rate in the mixed layer was allowed to be set. This necessitated a small change in the temperature profile between the mixed layer and the tropopause in order to keep the profile smooth. The $\frac{\partial\theta}{\partial z}$ term is calculated by using a user input temperature lapse rate and then using the hypsometric equation and the equation for potential temperature to solve for the potential temperature lapse rate.

The profile of relative humidity, H, is defined by

$$H(z) = \begin{cases} 1 - \frac{3}{4}\left(\frac{z}{z_{tr}}\right)^{5/4}, & z \leq z_{ml} \\ 1 - \frac{3}{4}\left(\frac{z - z_{ml}}{z_{tr} - z_{ml}}\right)^{13/16}, & z_{ml} < z \leq z_{tr} \\ 0.25, & z > z_{tr} \end{cases} \tag{2.4}$$

where variables carry the same meaning as in equation 2.3. Equation 2.4 has also been modified between the mixed layer and the tropopause. In this case the exponent on the second term was decreased from the value originally used in Weisman and Klemp (1982) and Weisman and Klemp (1984).

The modifications to the original analytic expressions were not made arbitrarily. There were specific reasons for the changes that will now be discussed. Through testing, it was found that surface vorticity values were

not approaching values seen in other numerical simulations. Comparing these other soundings with the canonical Weisman sounding showed a difference in low-level (i.e., within the PBL) lapse rates. Specifically, soundings with low-level lapse rates closer to dry adiabatic—indicative of a well-mixed PBL—produced higher surface vorticity values throughout their respective simulations. The Weisman sounding has an average low-level lapse rate of 7.5 K km^{-1}. Not surprisingly, it is more difficult to tilt horizontal vorticity into the vertical in a PBL that is less and less well-mixed (Parker, 2012). The PBL for these idealized simulations was set to be 9.6 K km^{-1}. With the lapse rates being set larger, the moisture profile was also modified so that it decreased more rapidly with height from the top of the mixed layer to the tropopause. This was done as too moist a profile, caused by a more gradual decrease in moisture with height, produced unrealistic looking convection.

A total of three buoyancy profiles are used with 1500 J kg^{-1}, 2500 J kg^{-1}, and 3500 J kg^{-1} of CAPE, respectively. Figure 2.3 is a plot of each profile plotted on skew-T log-P diagrams. The buoyancy in each sounding is maximized around the middle portion of a parcel's ascent. Differences in the vertical distribution of CAPE are known to have impacts on convection (McCaul and Weisman, 2001). Fortunately, in this study, the same general distribution of buoyancy throughout any parcel's ascent is seen in each profile. However, the 1500 J kg^{-1} case and, to some degree, the 2500 J kg^{-1} case do not have parcels that reach the tropopause level. While this does not match most observations, this is an artifact of the analytic functions used to create the profiles and was unavoidable. Another aspect to the profiles in Figure 2.3 is that the ML depth varies inversely with buoyancy. These changes in ML depth will likely affect the properties of downdrafts that develop within the simulated storms and will have to be kept in mind when interpreting results.

While this may seem concerning, these differences are observed in the real atmosphere which will still keep these results applicable in the real world.

Table 2.2 contains pertinent statistics extracted from the thermodynamic profiles in Figure 2.3. Corresponding MLCAPE and MLCIN values for all three CAPE cases are reported to get a better gauge of what the simulated storms encountered in their environment. The round number CAPE values will continue to be used for simplicity of naming. For all three CAPE cases, the statistics fall within the climatological range for the Great Plains in the spring (see Thompson et al., 2003; Grams et al., 2011). Regarding the variation in LCL and LFC across the three CAPE treatments, these differences will lead to differing results—something that has been simulated previously (McCaul and Cohen, 2002). Again, these differences occur in the real atmosphere and, given the degree to which these profiles are climatologically accurate, the results still can be generalized.

2.1.4 Convective initiation

Convection was initiated by adding positive perturbations to the base state potential temperature field in the initial model fields. Each of these perturbations had 8.5 km horizontal radii and 1.5 km vertical radii and were placed 1.5 km above the surface. Simulations could consist of either one thermal bubble (the control case) or two thermal bubbles (the experimental cases). The control thermal has a perturbation potential temperature of $\theta' = 3$ K whereas the experimental thermals all have $\theta' = 2$ K. Having differing θ' values simply ensures that the two simulated storms will have differing maturities when they interact. Interacting storms are commonly of differing maturity levels so this also increases the ability to generalize results to the real atmosphere.

In terms of bubble locations, this study takes a similar approach to Syrowski et al. (2012). All bubble locations are relative to the center of the domain. The control bubble is placed at $(x, y) = (0, 0)$ km. The experimental bubbles are placed at differing locations in each individual simulation. Figure 2.4 shows the layout of each thermal bubble in this study. Relative to the control storm, all secondary storms are initiated to the southwest (or, in Cartesian terms, the 3rd quadrant) relative to the control location. This decision was based on previous research (see Rogers and Weiss, 2008; Rogers, 2012; Syrowski et al., 2012) showing that interactions along the southwest flank of the main storm was typically stronger owing to relative lack of interference with either storms' inflow.

2.1.5 Data analysis

Output from the simulations was saved each minute. Three primary types of data were extracted from the output model fields for analysis: 1) 16 full-duration summary statistics, 2) domain-wide time series of 48 variables, and 3) time series data from 45 variables from the vicinity of tracked vorticity maxima. Analysis of these time series was done primarily with R (R Core Team, 2015).

Other analysis methods included plotting various model fields and inspecting the time series of those images. This work was primarily done using RIP (Stoelinga, 2013). Of particular interest in these images was to track storm mode through time of the simulations. Viewing animations of the model output also allowed features (e.g., vorticity maxima) to be tracked visually. This analysis gave a more physical context to the purely statistical look at the time series data. By physical context we mean that we can see each vorticity maxima's relative position to other features such as the

gust fronts or the primary updraft. From there, patters can emerge and be investigated further.

2.2 Tables

Model Parameter	Treatment
Microphysics	Morrison, 2-moment scheme (IHAIL = 1)
Radiation (Shortwave & Longwave)	Off
Surface Layer Scheme	Off
Land Surface Scheme	Off
PBL Scheme	Off
Friction	Off
Cumulus Parameterization	Off
Coriolis	Off
Time Integration Scheme	Runge-Kutta, 3rd order
6th Order Diffusion	On, up-gradient prohibited (Coeff. 0.1)
Damping	Rayleigh damping (5000 m depth, 0.2 s^{-1})
Horizontal Momentum Advection	5th order
Vertical Momentum Advection	3rd order
Horizontal Scalar Advection	5th order
Vertical Scalar Advection	3rd order
Moisture Advection	Monotonic
Scalar Advection	Monotonic
Turbulence & Mixing	3D Smagorinsky, 1st order closure

Table 2.1: WRF Model configurations used for idealized simulations.

Hodograph Parameter	Value
u_{sfc}	-5 m s^{-1}
v_{sfc}	4 m s^{-1}
U_s	25 m s^{-1}
V_s	20 m s^{-1}
S_u	0.5
S_v	0, 0.125, 0.25, 0.375, 0.5
a	0.5
d_c	1.5 km

Table 2.2: Settings used for idealized hodographs.

Shape Factor	0–1 km SRH	0–3 km SRH
0	30	80
0.125	47	98
0.25	73	130
0.375	98	169
0.5	124	176

Table 2.3: Hodograph SRH values for the 0–1 km and 0–3 km depths. SRH values are in units of m^2s^{-2}.

CAPE	**1500**	**2500**	**3500**
MLCAPE	1133	1991	3049
MLCIN	-10	-3	0
LCL	1431	1134	868
LFC	1781	1277	888
ML depth	1200	850	475

Table 2.4: Sounding statistics. CAPE, MLCAPE, and MLCIN are in units of J kg^{-1}. LCL, LFC, and ML depth are in units of m. To calculate MLCAPE and MLCIN the lowest 100 mb of the atmosphere was used to get the mixed parcel properties.

2.3 Figures

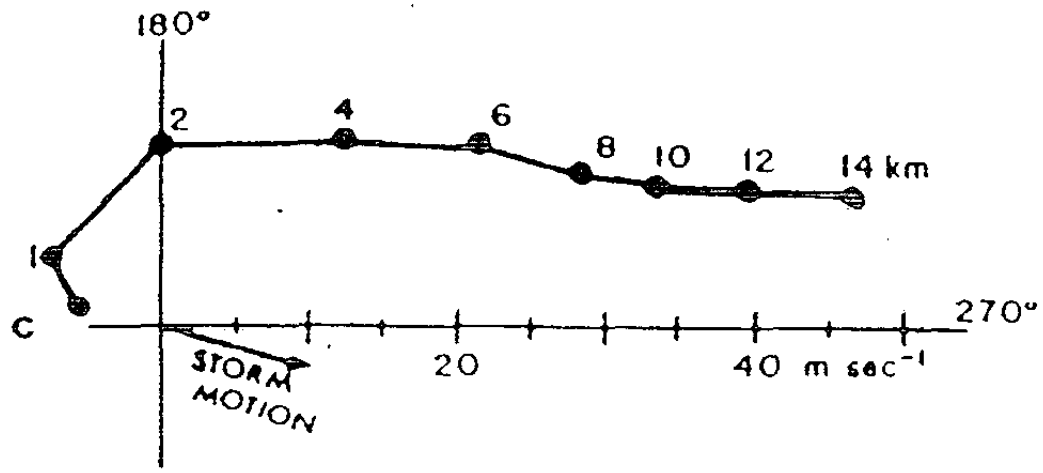

Figure 2.1: A hodograph typical of an environment supportive of supercelluar convection. Reproduced from Chisholm and Renick (1972).

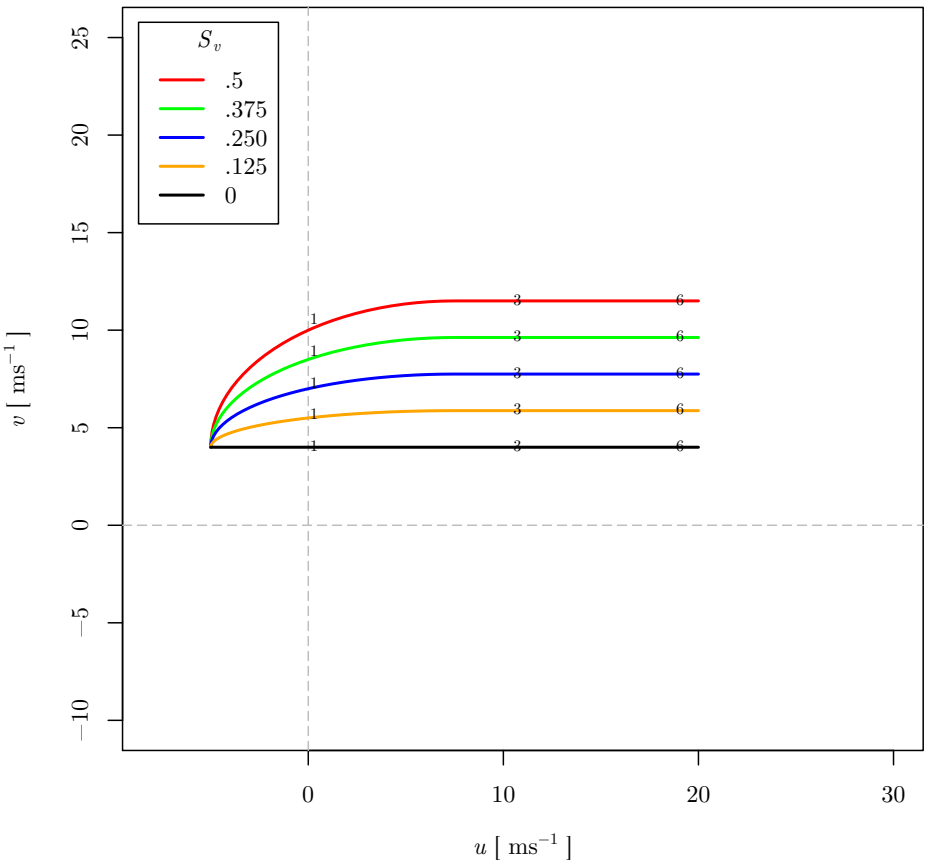

Figure 2.2: Idealized hodographs used for the matrix of storm interaction simulations. Hodographs are colored by their S_v values (see legend) and annotated with AGL heights (km).

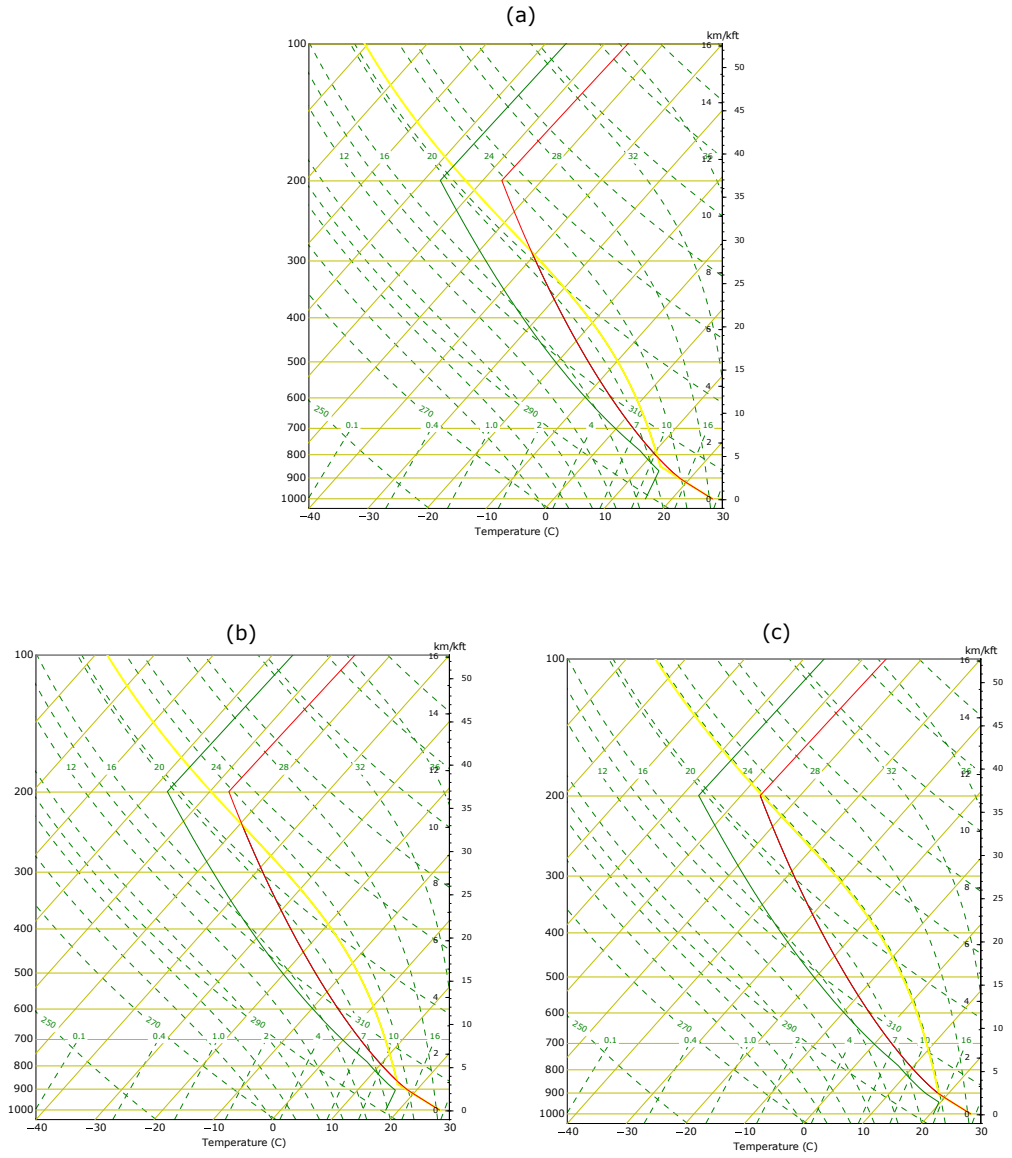

Figure 2.3: Idealized thermodynamic profiles used for the matrix of storm interaction simulations for (a) 1500 J kg^{-1}, (b) 2500 J kg^{-1}, and (c) 3500 J kg^{-1} of CAPE. The parcel process curve for a mixed parcel (lowest 100 mb) is shown in solid yellow.

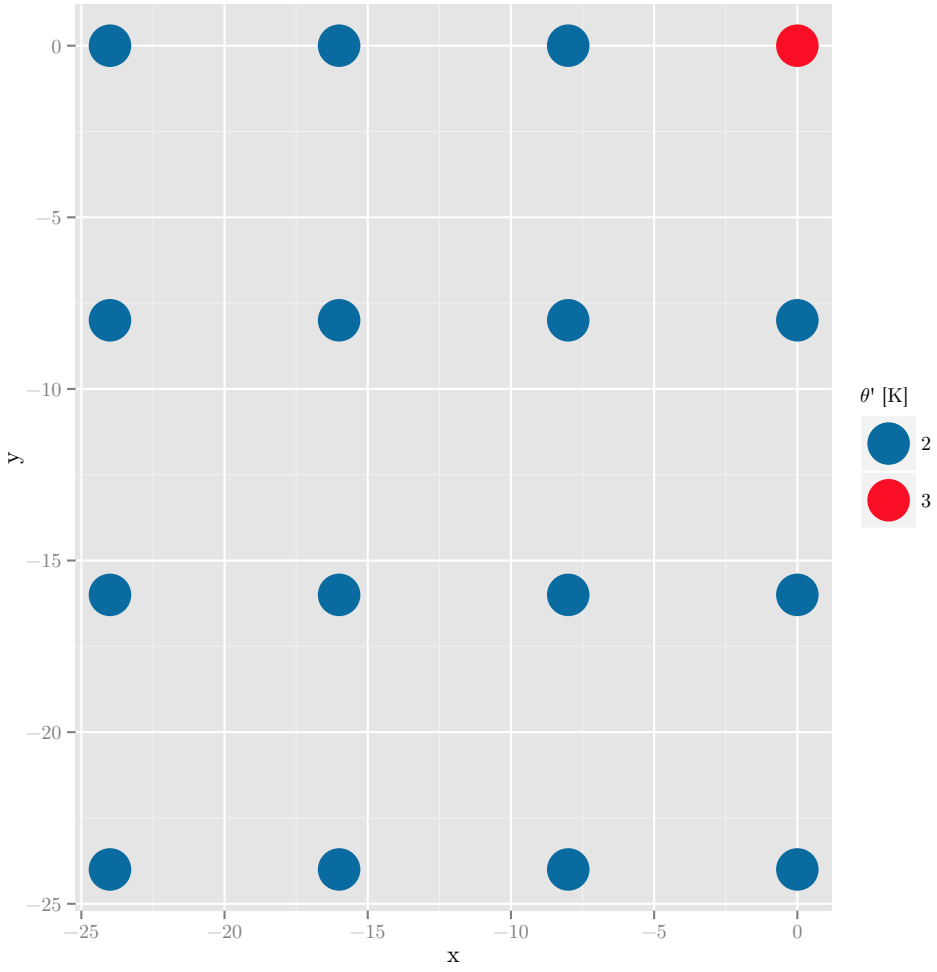

Figure 2.4: Locations of all θ perturbation bubbles used in this study. The control bubble (red) is always located at $(x, y) = (0, 0)$ km and has $\theta' = 3$ K. The experimental bubbles (blue) change location in each simulation and have $\theta' = 2$ K. Each bubble is spaced 8 km from the next. Grid coordinates are domain-center relative and represent distance in km.

3 Results

3.1 Control runs

The control cases that were simulated in this study provide an important baseline the two-thermal cases, hereafter experimental runs, will be compared to. Figure 3.1 shows simulated reflectivity for several simulations after 2 hours of computation. The 1500 J kg^{-1} runs appear on top with CAPE increasing downward. The no curvature runs appear on the left with the full QSC curvature on the right. What is seen in Figure 3.1 is that all of the right-moving (southernmost) storms have a mature, supercellular structure. Some convection has developed between the right-moving and left-moving (largest northernmost) supercells. As CAPE increases, come elevated convection tends to develop within the outflow region from the parent storms. Beyond 2 hours of simulation time, convection grows upscale and becomes more linear with the right-moving supercell still tending to be present along the southern edge of the line.

Figures 3.2, 3.3, and 3.4 compare maximum surface vorticity of all control cases and all experimental cases for 1500 J kg^{-1}, 2500 J kg^{-1}, and 3500 J kg^{-1} CAPE, respectively. Please note the differing scales on the y-axis. The most obvious feature of these figures is the experimental runs have higher surface vorticity than the control cases starting relatively early. The dominance of the experimental runs lasts until about 100 minutes into the simulations. Beyond 100 minutes, the control cases tend to have much higher variance

in surface vorticity as well as trending more toward values in the middle of the experimental runs range. Control runs also have maximum surface vorticity magnitudes that generally peak around 3500–4500 $\times$ 10^{-5} s^{-1}. A secondary feature of the control runs is that they are often not the weakest of the simulations in their respective groups.

3.2 Experimental runs

3.2.1 General character

The general character of the two-cell storm simulations were different than the control simulations in most cases. When the cell separation between the two storms was very small (around 8 km), the storm interactions occurred very early and the updrafts of the two storms merged together quickly leaving one discrete storm. In these cases the discrete cell from the two merged cells behaved much like a control simulation. However, the merged storm was often stronger than the single-cell control simulations. For cell separation distance that was beyond 8 km, the two storms would stay independent for a much longer time. With time, convection would grow upscale and become more linear. However, it was often the case that the southern-most cell retained at least some of its supercellular structure. The most interesting finding with regard to storm character in the two-cell storm simulations is that there was a wide degree of variation between storms in one buoyancy and shear profile to storms in another. Even as early as 120 minutes into the simulation, you would see some two-cell simulations retaining much more supercellular structure while others were already quite linear.

3.2.2 Storm mode trends

The dominant storm mode between one and two hours simulation time was examined for any patterns across the parameter space. Control storms were not considered in this analysis as they were nearly all classic supercells. Figure 3.5 shows the distribution of storm modes for each shear treatment. There is a clear trend in both classic supercells (CL) and linear modes (LN). Specifically, more CL and LN storms occur as the shear level is increased. The amount of high-precipitation (HP) storms remains roughly static. Figure 3.6 is similar to Figure 3.5 only the storm type distribution is shown for each CAPE treatment. Here, a trend in CL and LN storms is also evident; however, this time CL storms decrease and LN storms increase as the CAPE level is increased. Again, the HP numbers are roughly static.

The most interesting trend becomes clear when storm type distribution is examined as a function of relative direction away from the control thermal (Figure 3.7). HP storms are favored when a second storm exists to the southwest of the control. CL storms are most favored when the second cell exists directly to the south of the control cell. To the west, south-southwest, and west-southwest the distributions of CL and HP storms are generally more equal.

3.2.3 Migrating vorticity maxima

A ubiquitous feature in these simulations were vorticity maxima that would, at times, move along the gust front boundaries. The strongest migrating maxima existed along the forward flank gust front (FFGF). Where the vorticity maxima ultimately ended up was dictated by the location of the gust fronts of the two cells. When gust fronts from both cells were not favorably

aligned, the migrating vorticity maxima were less likely to move underneath an updraft, stretch, and intensify. An example of this set up can be seen in Figure 3.8. There the gust fronts have a discontinuity and the vorticity maxima tend not to interact with the other storm in this scenario. However, gust fronts that exhibited a more favorable alignment tended to have several migrating vorticity maxima that interacted with the updraft of one of the storm cells. An example of this can be seen in Figure 3.9. There the gust fronts of the two storms are continuous and the vorticity maxima readily migrate from the northern storm's FFGF to the southern storm's FFGF and updraft. Even given a favorable gust front orientation, the vorticity maxima did not invariably reach an updraft. Storms with stronger gust fronts and, by extension, cold pools, had gust fronts that would surge out and undercut the updrafts. When this occurred the vorticity maxima would continue to migrate down the gust front, but be too far removed from the updraft to interact with it.

3.3 Figures

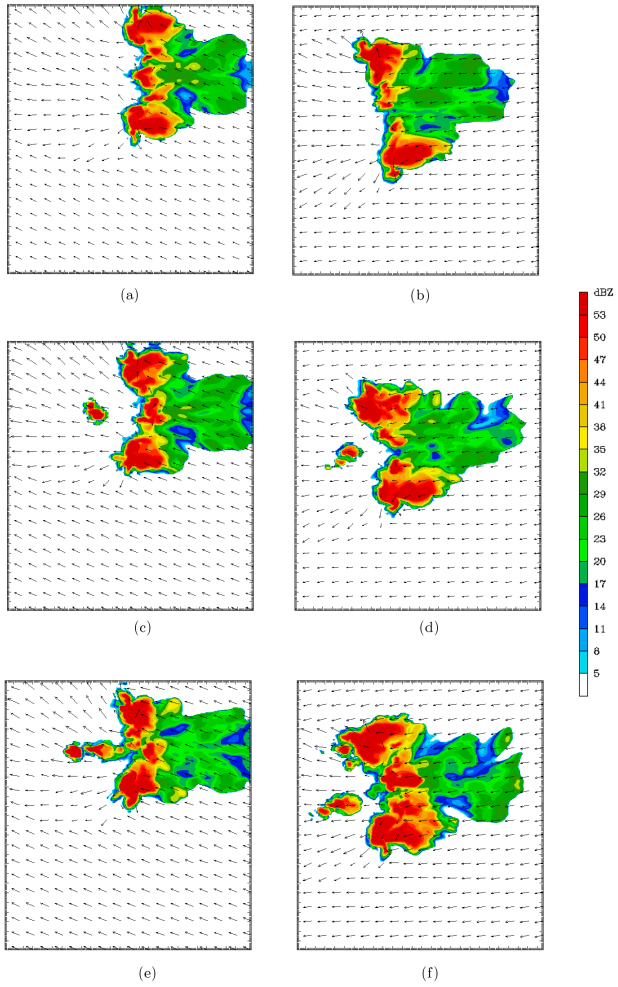

Figure 3.1: Simulated reflectivity at 1 km AGL (dBZ, see legend) and surface storm-relative winds (vectors) for simulation time $t = 2$ hours. The left column (a), (c), (e) represents the straight hodograph simulations for CAPE cases of (a) 1500 J kg^{-1}, (c) 2500 J kg^{-1}, and (e) 3500 J kg^{-1}. The right column (b), (d), and (f) represents the QSC hodograph simulations for CAPE cases of (b) 1500 J kg^{-1}, (d) 2500 J kg^{-1}, and (f) 3500 J kg^{-1}. For spatial reference, every major tick mark represents 5.4 km.

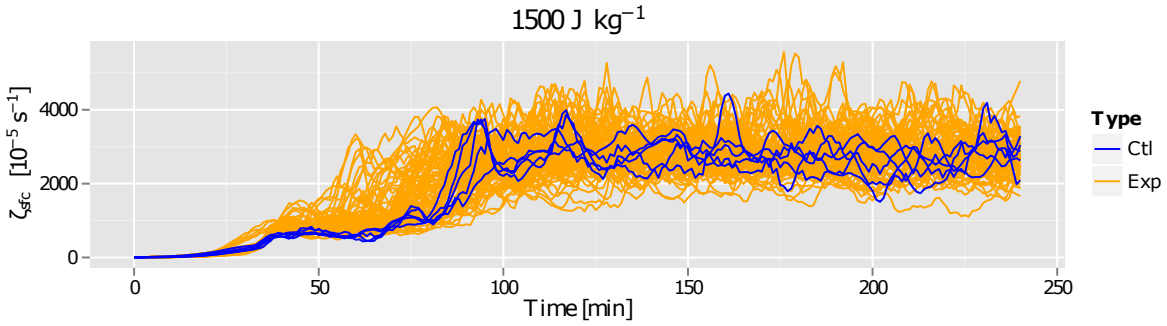

Figure 3.2: Max surface vorticity (ζ_{sfc}, 10^{-5} s^{-1}) for the 1500 J kg^{-1} CAPE case over all shear treatments. Control (ctl) cases are in blue and experimental (exp) cases are in orange.

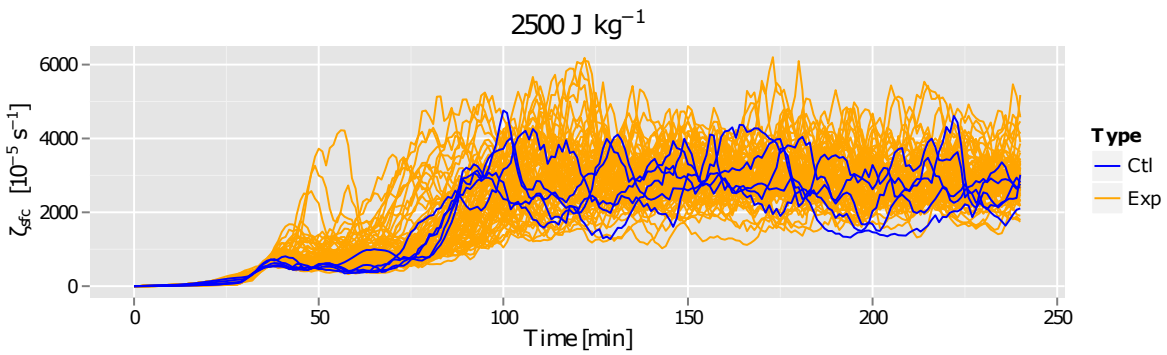

Figure 3.3: Max surface vorticity (ζ_{sfc}, 10^{-5} s^{-1}) for the 2500 J kg^{-1} CAPE case over all shear treatments. Control (ctl) cases are in blue and experimental (exp) cases are in orange.

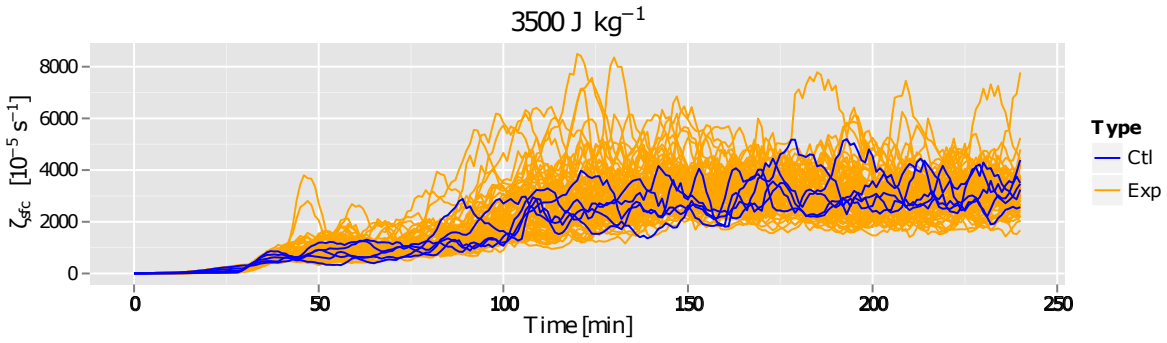

Figure 3.4: Max surface vorticity (ζ_{sfc}, 10^{-5} s^{-1}) for the 3500 J kg^{-1} CAPE case over all shear treatments. Control (ctl) cases are in blue and experimental (exp) cases are in orange.

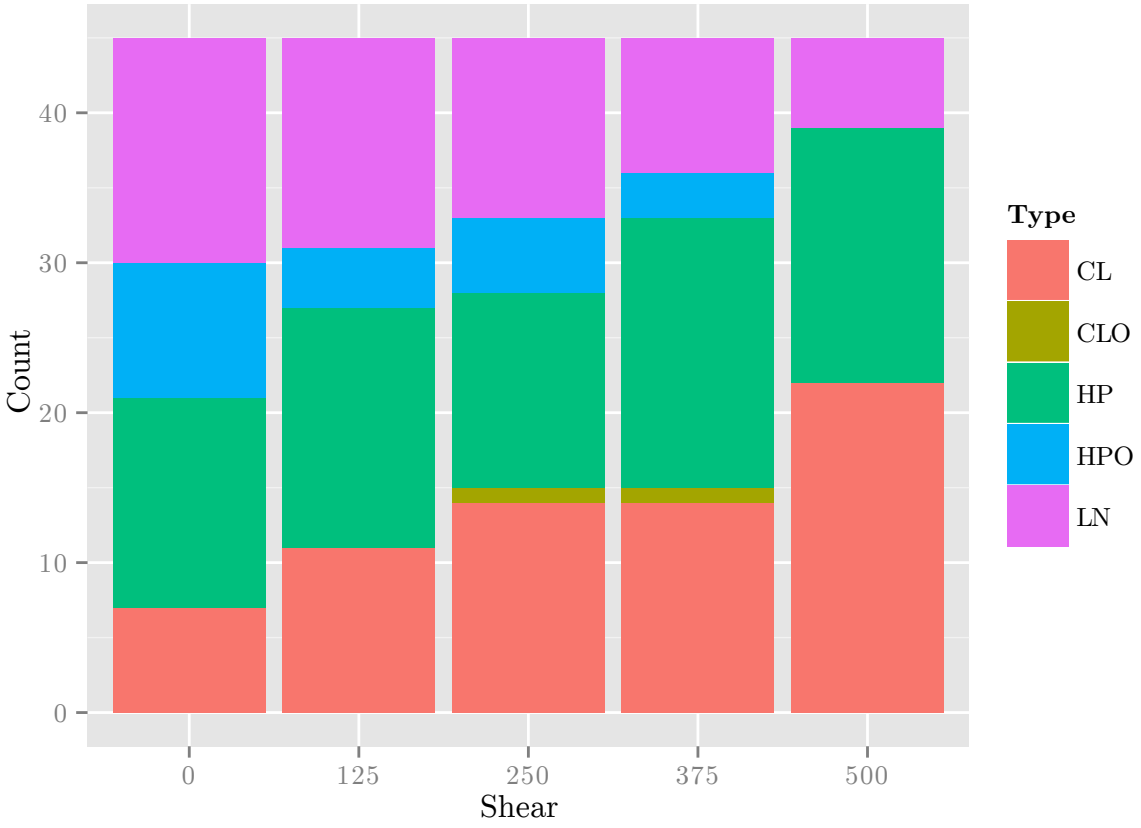

Figure 3.5: Storm type by shear treatment. Shear is on the x-axis and increases from the straight hodograph case (0) to the quarter semi-circle case (500). Count of the storm type is on the y-axis. Storm types are classic supercell (CL), high-precipitation (HP), and linear (LN). Outflow dominant sub-categories are denoted by an appended "O".

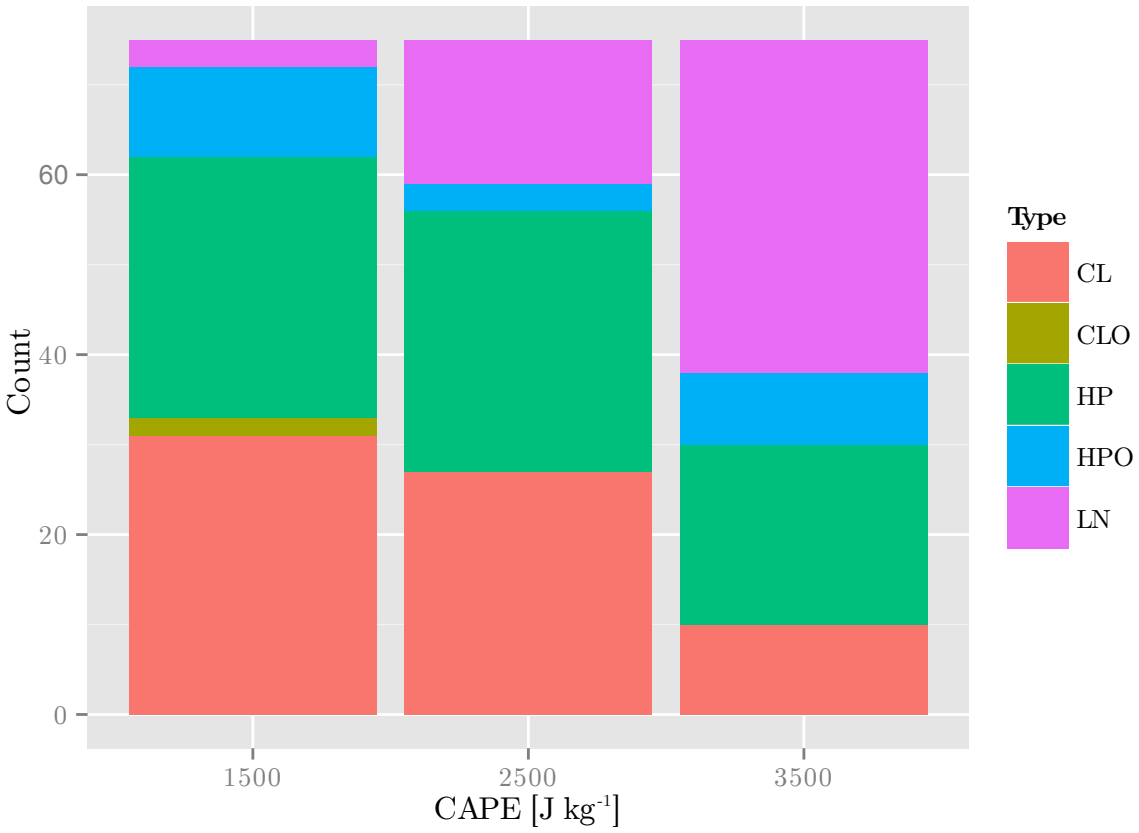

Figure 3.6: Storm type by CAPE treatment. CAPE is on the x-axis. Count of the storm type is on the y-axis. Storm types are classic supercell (CL), high-precipitation (HP), and linear (LN). Outflow dominant sub-categories are denoted by an appended "O".

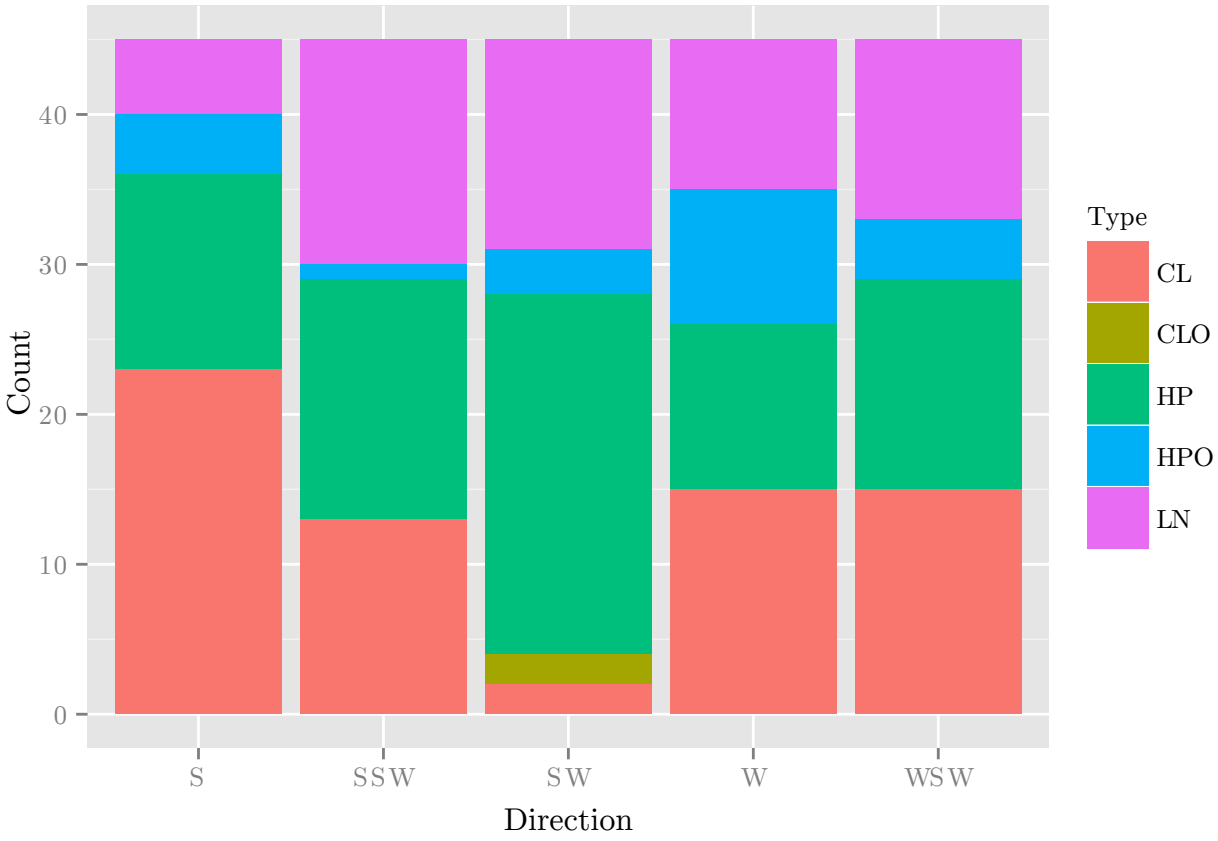

Figure 3.7: Storm type by direction relative to the single cell control thermal location. Control-relative direction is on the x-axis. Count of the storm type is on the y-axis. Storm types are classic supercell (CL), high-precipitation (HP), and linear (LN). Outflow dominant sub-categories are denoted by an appended "O".

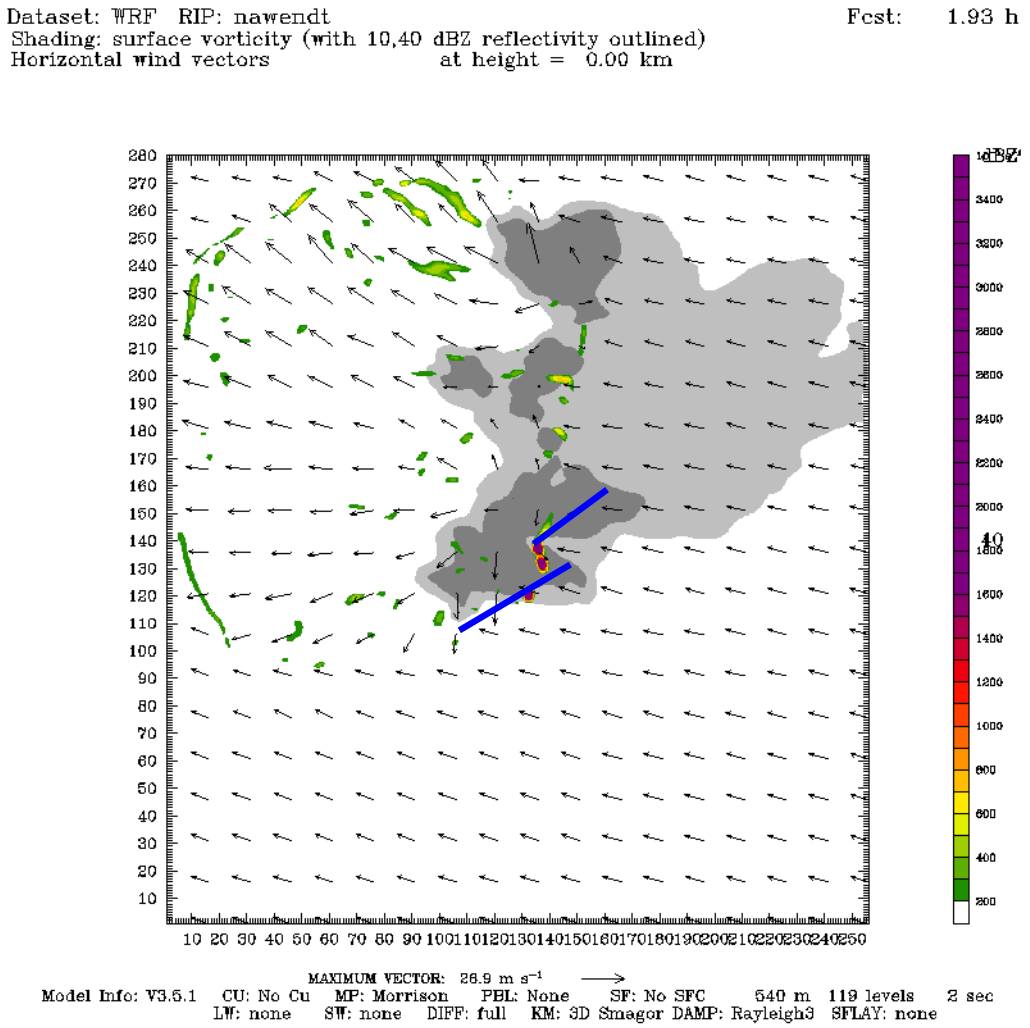

Figure 3.8: An exmple of a unfavorable gust front (blue lines) orientation taken from the 1500 J kg^{-1} CAPE, 125 shear, $x, y = -16, -16$ case at 1 hour into the simulation. 1 km simulated reflectivity (dBZ) shaded at 10 dBZ (light gray) and 40 dBZ (dark gray). Surface vertical vorticity (10^{-5} s^{-1};color fill starting at 200 10^{-5} s^{-1}) and storm-relative winds (vectors).

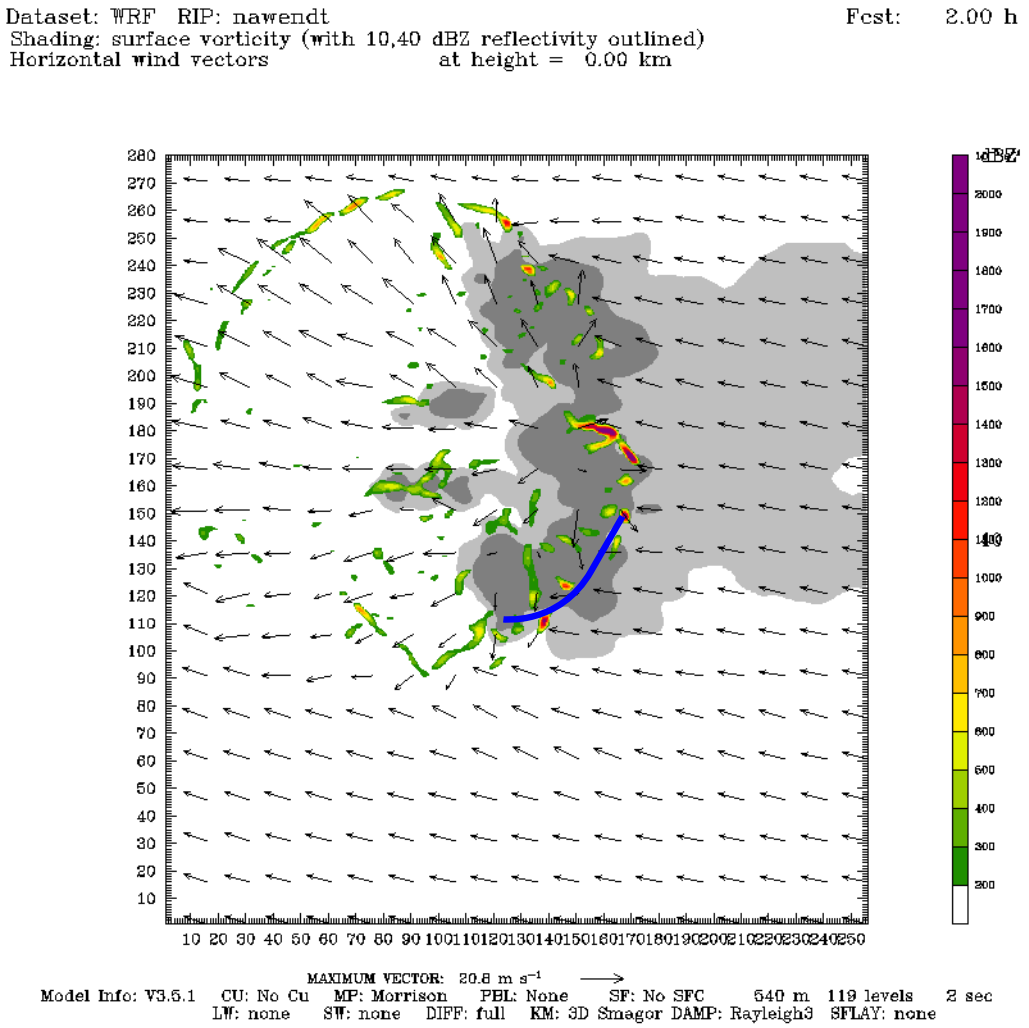

Figure 3.9: An exmple of a favorable gust front (blue line) orientation taken from the 3500 J kg^{-1} CAPE, 125 shear, $x, y = 0, -24$ case at 1 hour into the simulation. 1 km simulated reflectivity (dBZ) shaded at 10 dBZ (light gray) and 40 dBZ (dark gray). Surface vertical vorticity (10^{-5} s^{-1};color fill starting at 200 10^{-5} s^{-1}) and storm-relative winds (vectors).

4 Discussion & Conclusions

Simulations showed a wide degree of variability—both the single storm and the two storm cases. What is of particular interest is the variability of the control simulations. As was seen in Figures 3.2, 3.3, and 3.4, the control simulations were not the overall weakest in terms of intensity of surface rotation. This is in direct contrast to the findings of Syrowski et al. (2012) where the control run was the weakest. Much of the difference between the current study and that of Syrowski et al. is due to the use of several soundings to initialize the model versus only one. In some environments, the single, isolated storms may exhibit the lowest surface vertical vorticity values. Given a variable environment, however, the control storms may have more intense rotation while situations with a secondary storm will be weaker due to destructive interference between the two storms.

A pattern that emerged when viewing the time evolution of the surface vertical vorticity field indicated that the alignment of the gust fronts in the two storm simulations was important for intensification of the surface vorticity maxima. Gust fronts from two storms that were more favorably aligned (i.e., continuous) increased the likelihood of the surface vertical vorticity maxima migrating underneath an updraft and being stretched and intensified. The pertinent physical mechanisms in this situation can be described

the labeled terms in equation 4.1.

$$\frac{d(\zeta + f)}{dt} = \underbrace{-\nabla \cdot (\zeta + f)}_{\text{Divergence}} - \left(\frac{\partial w}{\partial x}\frac{\partial v}{\partial z} - \frac{\partial w}{\partial y}\frac{\partial u}{\partial z} \right) + \underbrace{\frac{1}{\rho^2}\left(\frac{\partial \rho}{\partial x}\frac{\partial p}{\partial y} - \frac{\partial \rho}{\partial y}\frac{\partial p}{\partial x} \right)}_{\text{Solenoidal}} \tag{4.1}$$

This equation is the vertical vorticity equation in height coordinates. The divergence and solenoidal terms are labeled. An interaction between two boundaries as shown in Figure 3.9 can lead to an increase in convergence and baroclinicity (read: density gradients) which, by equation 4.1, leads to an increase in vertical vorticity. This phenomenon has also been documented in nature. Wolf and Szoke (1996) described two storms‘ gust fronts interacting with one another and a tornado occurring shortly thereafter (Figure 4.1). Wolf and Szoke posited the same mechanism as above as the catalyst for the tornado.

An analysis of the storm mode across the CAPE and shear treatments showed some interesting trends (Figures 3.5, 3.6, and 3.7). With increasing shear, the amount of classic supercells grew larger. Since only low level shear was changed, the most likely explanation for this behavior is the suppression of the left split supercell storms due to the unfavorable perturbation pressure gradient induced by the wind profile (Rotunno and Klemp, 1982). The suppression of the left movers helped to keep interactions to a minimum and allow storms to remain more discrete for longer. As CAPE increased, the LN storms were more prevalent and CL storms decreased in frequency.

This study examined the role of varying environmental shear and buoyancy on the relationship between storm interactions and storm morphology and intensity. Significant amounts of variation in overall storm evolution

and intensity were seen across all of the simulations. Gust fronts of two distinct storms that interacted favorably increased the likelihood of discrete areas of surface vertical vorticity to be ingested into and stretched by a storm's updraft. Higher shear simulations were more likely to produce CL storms whereas higher CAPE simulations were more likely to produce less CL storms. Simulations with a secondary storm to the SW of the control cell tended to be much more HP in character.

A great deal of data was produced in this study. Many questions linger after traditionally used statistics and techniques were not able to elucidate many patterns in the data. Some preliminary work using self-organizing maps (SOM; Kohonen, 2001, 2013) has been done. Using a artificial neural network such as the SOM helps to find patterns in the data that are hard to recognize with traditional methods of analysis. Trajectory analysis will also be a part of future work on this data. Trajectories will help provide physical links between the air parcels impacted by one storm that my interact with another storm. Other interesting work has been done using machine learning techniques applied to meteorological data. McGovern et al. (2014) used spatiotemporal statistics to identify arbitrary 2D and 3D shapes in numerical weather simulations. These techniques are a great tool when looking for pattern in the shape or orientation of important features in weather simulations. Much can be done to continue mining these data for more insight on how storm interactions may work in the real atmosphere.

4.1 Figures

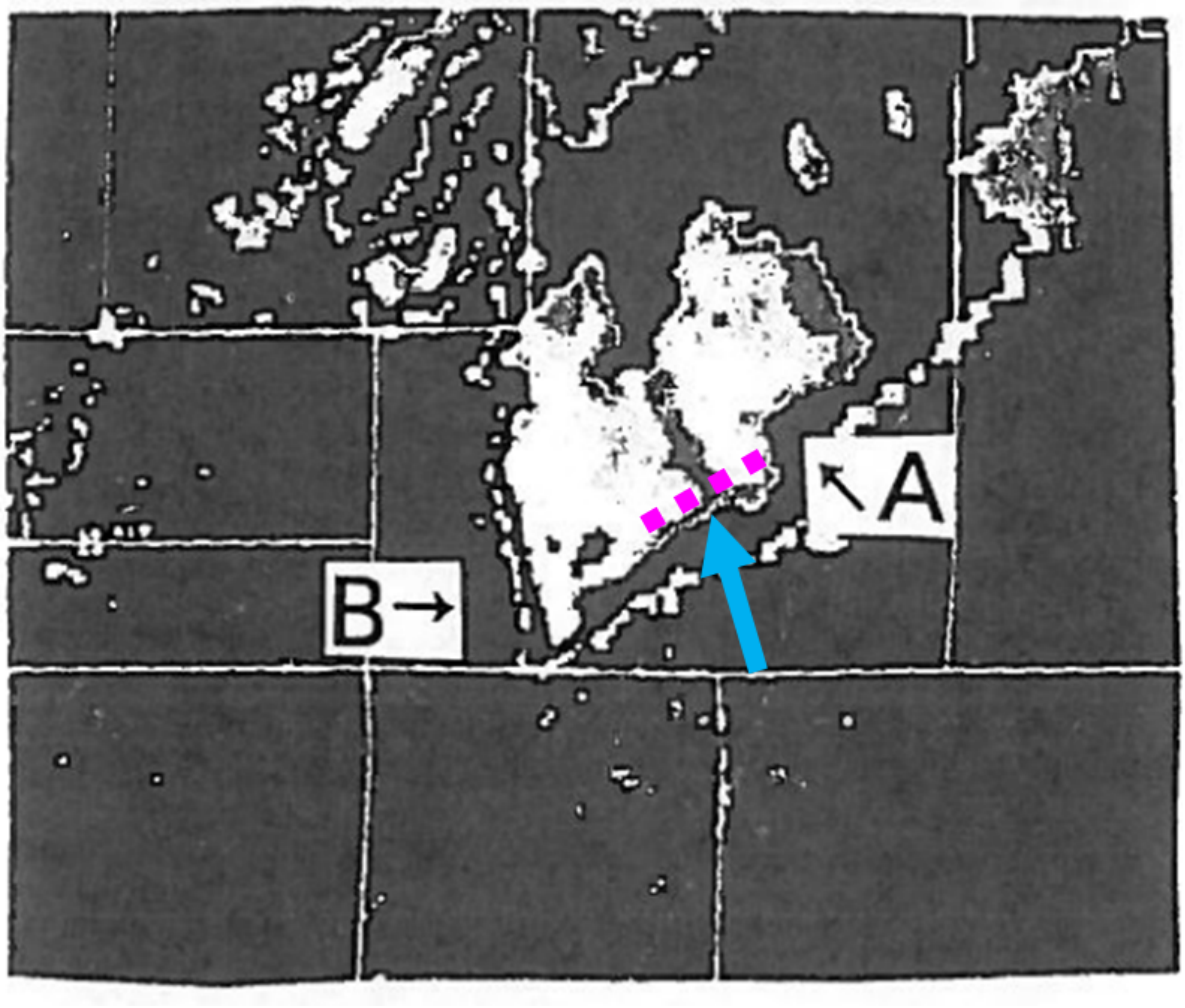

Figure 4.1: NCAR Mile-Hi radar refelectivity at 0.5° elevation angle. Interacting gust fronts highlighted with magenta dashed line. Figure adapted from Wolf and Szoke (1996).

References

Arakawa, A., and V. R. Lamb, 1977: Computational design of the basic dynamical processes of the UCLA general circulation model. *Methods in Computational Physics: Advances in Research and Applications*, J. Chang, Ed., Vol. 17, Academic Press, New York, 173–265.

Bluestein, H. B., and M. L. Weisman, 2000: The interaction of numerically simulated supercells initiated along lines. *Mon. Wea. Rev.*, **128 (9)**, 3128–3149.

Chisholm, A. J., and J. H. Renick, 1972: The kinematics of multicell and supercell Alberta hailstorms. Alberta Hail Studies, Rep. 72-2, Research Council of Alberta Hail Studies, Edmonton, Canada, 24-31 pp.

Davies-Jones, R., 1984: Streamwise vorticity: The origin of updraft rotation in supercell storms. *J. Atmos. Sci.*, **41 (20)**, 2991–3006.

Doswell, C. A., S. J. Weiss, and R. H. Johns, 1993: Tornado forecasting: a review. *The Tornado: Its Structure, Dynamics, Prediction, and Hazards*, American Geophysical Union, 557–571.

French, A. J., and M. D. Parker, 2012: Observations of mergers between squall lines and isolated supercell thunderstorms. *Wea. Forecasting*, **27 (2)**, 255–278.

Gilmore, W. T., and N. I. Fox, 2005: Observations of supercell merger and tornadogenesis from May 4, 2003. *32nd Conference on Radar Meteorology*, Amer. Met. Soc., Albuquerque, NM, P15R.10, URL http://ams.confex.com/ams/32Rad11Meso/webprogram/Paper96526.html.

Goodman, S. J., and K. R. Knupp, 1993: Tornadogenesis via squall line and supercell interaction: the november 15, 1989, huntsville, alabama, tornado. *The Tornado: Its Structure, Dynamics, Prediction, and Hazards*, C. Church, D. Burgess, C. Doswell, and R. Davies-Jones, Eds., American Geophysical Union, 183–199.

Grams, J. S., R. L. Thompson, D. V. Snively, J. A. Prentice, G. M. Hodges, and L. J. Reames, 2011: A climatology and comparison of parameters for significant tornado events in the united states. *Wea. Forecasting*, **27 (1)**, 106–123.

Hastings, R. M., 2013: Long-term morphological changes in mature supercells following mergers with nascent cells in environments with directionally-varying shear. Ph.D. thesis, The Pennsylvania State University, 155 pp.

Hastings, R. M., and Y. P. Richardson, 2010: Storm mergers. Part I: Preliminary numerical investigation of merger events. *25th Conference on Severe Local Storms*, Amer. Met. Soc., Denver, CO, 7A.5, URL http://ams.confex.com/ams/25SLS/webprogram/Paper176048.html.

Hastings, R. M., Y. P. Richardson, and P. M. Markowski, 2012: Mergers in supercell environments. Part II: Tornadogenesis potential during merger as evaluated by changes in the near-surface low-level mesocyclone. *26th Conference on Severe Local Storms*, Amer. Met. Soc., Nashville, TN, 143, URL http://ams.confex.com/ams/26SLS/webprogram/Paper212519.html.

Hastings, R. M., Y. P. Richardson, and P. M. Markowski, 2014: Simulation of near-surface mesocyclogenesis during mergers between mature and nascent supercells. *27th Conference on Severe Local Storms*, Amer. Met. Soc., Madison, WI, 3B.2, URL http://ams.confex.com/ams/27SLS/webprogram/Paper255837.html.

Hastings, R. M., Y. P. Richardson, and J. Wurman, 2010: Storm mergers. Part II: Observations of merger events from VORTEX2. *25th Conference on Severe Local Storms*, Amer. Met. Soc., Denver, CO, P8.16, URL http://ams.confex.com/ams/25SLS/webprogram/Paper176073.html.

Heymsfield, G. M., R. Fulton, and J. D. Spinhirne, 1991: Aircraft overflight measurements of midwest severe storms: Implications an geosynchronous satellite interpretations. *Mon. Wea. Rev.*, **119 (2)**, 436–456.

Jewett, B. F., R. W. Przybylinsky, and R. B. Wilhelmson, 2006: Numerical simulation of the 24 April, 2002 storm merger between a left moving storm and supercell. *23rd Conference on Severe Local Storms*, Amer. Met. Soc., St. Louis, MO, P11.3, URL http://ams.confex.com/ams/23SLS/webprogram/Paper115478.html.

Jewett, B. F., R. B. Wilhelmson, and B. D. Lee, 2002: Numerical simulation of cell interaction. *21st Conference on Severe Local Storms*, Amer. Met. Soc., San Antonio, TX, P6.6, URL http://ams.confex.com/ams/SLS_WAF_NWP/webprogram/Paper47219.html.

Knievel, J. C., G. H. Bryan, and J. P. Hacker, 2007: Explicit numerical diffusion in the wrf model. *Mon. Wea. Rev.*, **135 (11)**, 3808–3824.

Kohonen, T., 2001: *Self-organizing maps*. 3rd ed., Springer, New York.

Kohonen, T., 2013: Essentials of the self-organizing map. *Neural Networks*, **37**, 52–65.

Lee, B. D., B. F. Jewett, and R. B. Wilhelmson, 2006: The 19 April 1996 Illinois tornado outbreak. Part II: Cell mergers and associated tornado incidence. *Wea. Forecasting*, **21 (4)**, 449–464.

Lindsey, D. T., and M. J. Bunkers, 2004: On the motion and interaction between left- and right-moving supercells on 4 May 2003. *22nd Conference on Severe Local Storms*, Amer. Met. Soc., Hyannis, MA, 12.1, URL http://ams.confex.com/ams/11aram22sls/techprogram/paper_81463.htm.

McCaul, E. W., and C. Cohen, 2002: The impact on simulated storm structure and intensity of variations in the mixed layer and moist layer depths. *Mon. Wea. Rev.*, **130 (7)**, 1722–1748.

McCaul, E. W., and M. L. Weisman, 2001: The sensitivity of simulated supercell structure and intensity to variations in the shapes of environmental buoyancy and shear profiles. *Mon. Wea. Rev.*, **129 (4)**, 664–687.

McGovern, A., I. Gagne, DavidJ, J. Williams, R. Brown, and J. Basara, 2014: Enhancing understanding and improving prediction of severe weather through spatiotemporal relational learning. *Mach Learn*, **95 (1)**, 27–50.

Morrison, H., J. A. Curry, and V. I. Khvorostyanov, 2005: A new double-moment microphysics parameterization for application in cloud and climate models. part i: Description. *J. Atmos. Sci.*, **62 (6)**, 1665–1677.

Parker, M. D., 2012: Impacts of lapse rates on low-level rotation in idealized storms. *J. Atmos. Sci.*, **69 (2)**, 538–559.

Parker, M. D., 2014: Composite VORTEX2 supercell environments from near-storm soundings. *Mon. Wea. Rev.*, **142 (2)**, 508–529.

R Core Team, 2015: *R: A Language and Environment for Statistical Computing*. Vienna, Austria, R Foundation for Statistical Computing, URL http://www.R-project.org/.

Rasmussen, E. N., 2003: Refined supercell and tornado forecast parameters. *Wea. Forecasting*, **18 (3)**, 530–535.

Rasmussen, E. N., and D. O. Blanchard, 1998: A baseline climatology of sounding-derived supercell and tornado forecast parameters. *Wea. Forecasting*, **13 (4)**, 1148–1164.

Rogers, J. W., 2012: Significant tornado events associated with cell mergers. *26th Conference on Severe Local Storms*, Amer. Met. Soc., Nashville, TN, 9.4, URL http://ams.confex.com/ams/26SLS/webprogram/Paper211575.html.

Rogers, J. W., and C. C. Weiss, 2008: The association of cell mergers with tornado occurrence. *24th Conferecne on Severe Local Storms*, Amer. Met. Soc., Savannah, GA, P3.23, URL http://ams.confex.com/ams/24SLS/webprogram/Paper141784.html.

Rotunno, R., and J. B. Klemp, 1982: The influence of the shear-induced pressure gradient on thunderstorm motion. *Mon. Wea. Rev.*, **110 (2)**, 136–151.

Rotunno, R., J. B. Klemp, and M. L. Weisman, 1988: A theory for strong, long-lived squall lines. *J. Atmos. Sci.*, **45 (3)**, 463–485.

Skamarock, W., and Coauthors, 2008: A description of the Advanced Research WRF Version 3. NCAR Tech. Note NCAR/TN475+STR.

Stoelinga, M. T., 2013: *RIP: A Program for Visualizing Mesoscale Model Output*. Seattle, Washington, University of Washington, URL http://www2.mmm.ucar.edu/wrf/users/docs/ripug.htm.

Syrowski, A., B. F. Jewett, and R. B. Wilhelmson, 2012: An assessment of internal and external forcings in supercell interactions and their impact on storm morphology. *26th Conference on Severe Local Storms*, Amer. Met. Soc., Nashville, TN, 11B.5, URL http://ams.confex.com/ams/26SLS/webprogram/Paper212183.html.

Tanamachi, R. L., P. L. Heinselman, and L. J. Wicker, 2015: Impacts of a storm merger on the 24 may 2011 el reno, oklahoma, tornadic supercell. *Weather and Forecasting*, **30 (3)**, 501–524.

Tao, W.-K., and J. Simpson, 1989: A further study of cumulus interactions and mergers: Three-dimensional simulations with trajectory analyses. *J. Atmos. Sci.*, **46 (19)**, 2974–3004.

Thompson, R. L., R. Edwards, J. A. Hart, K. L. Elmore, and P. Markowski, 2003: Close proximity soundings within supercell environments obtained from the rapid update cycle. *Wea. Forecasting*, **18 (6)**, 1243–1261.

Van Leer, K. W., 2012: Rapid intensification mechanisms including the role of storm mergers in the 22 may 2011 joplin, mo tornadic storm. *26th Conference on Severe Local Storms*, Amer. Met. Soc., Nashville, TN, 6.2, URL http://ams.confex.com/ams/26SLS/webprogram/Paper211986.html.

Weisman, M. L., and J. B. Klemp, 1982: The dependence of numerically simulated convective storms on vertical wind shear and buoyancy. *Mon. Wea. Rev.*, **110 (6)**, 504–520.

Weisman, M. L., and J. B. Klemp, 1984: the structure and classification of numerically simulated convective storms in directionally varying wind shears. *Mon. Wea. Rev.*, **112 (12)**, 2479–2498.

Weisman, M. L., and R. Rotunno, 2000: The use of vertical wind shear versus helicity in interpreting supercell dynamics. *J. Atmos. Sci.*, **57 (9)**, 1452–1472.

Wolf, R., and E. Szoke, 1996: The multiscale analysis of the 21 july 1993 northeast colorado tornadoes. *Preprints, 18th Conference on Severe Local Storms*, Amer. Met. Soc., San Francisco, CA, 403–407.

Wurman, J., Y. Richardson, C. Alexander, S. Weygandt, and P. F. Zhang, 2007: Dual-doppler and single-doppler analysis of a tornadic storm undergoing mergers and repeated tornadogenesis. *Mon. Wea. Rev.*, **135 (3)**, 736–758.